Scattering of internal waves over random topography

Yuan Guo

September 30, 2012

1 Introduction

Internal waves are initially generated as the barotropic tides (described by $\mathbf{U}(t) = \hat{\mathbf{x}} U_0 \cos \omega t$) flow over undulating sea-floor topography. They are an important component in ocean dynamics such as small-scale mixing and dissipation. Internal waves generated by barotropic tides are usually of low mode number so they are of large-scale. Where are those small-scale waves come from? One possible way of generating these small-scale waves is scattering (See Figure 1). Scattering is a linear interaction between the propagating waves and the sea-floor

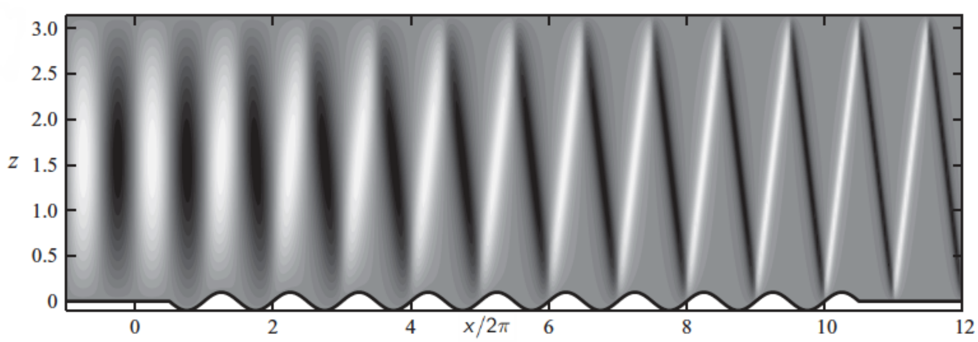

Figure 1: Snapshot at $t = 0$ of $\mathrm{Re}\Psi(x, z)e^{-it}$ for topography $h(x) = 0.1 \sin x$. It is clear from the graph that the width of white or black region (represent the scale of the waves) changes from large to small. This Figure is taken from Bühler & Holmes-Cerfon, 2011

topography. The rugged bottom topography scatters the incoming waves into other spectral modes and redistributes energy flux in the waves number space. Figure 2 is an example of scattering. The incoming waves we use is of mode-one and we can see that by scattering we obtain waves with high-wave number. Details of this redistribution process depend on the shape of the topography, i.e. whether it is subcritical or supercritical (see definition below Equation (7)).

Scattering problem is studied for determined topography by Mülcer & Liu (1999) and subcritical random topography (Section 2.2) by Bühler & Holmes-Cerfon (2011). Here we want to know what will happen when we allow random topography to have supercritical part.

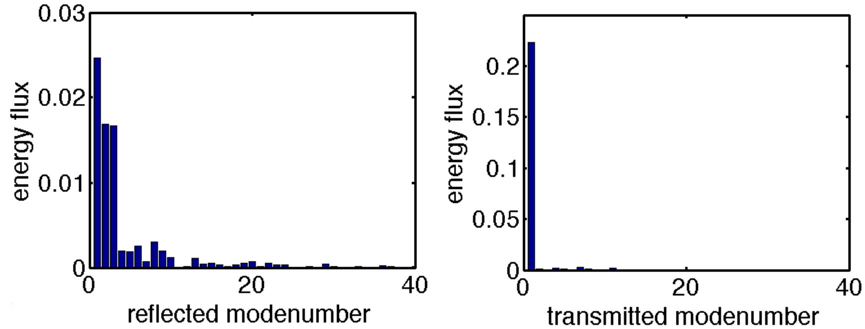

Figure 2: An example of scattering of internal waves. The incoming waves are of mode-one and with energy flux rescaled to unity. We only plot energy flux of the first 40 modes.

In this paper, we study two-dimensional (2D) scattering problem for ocean with finite depth by using linearized two-dimensional (2D) rotating Boussinesq system. Linearization is justified if the tidal excursion is much less than the scale of the topography. For simplicity, the Coriolis frequency f and the buoyancy frequency N are taken to be constants, though N is a function of depth z in real ocean. However, previous experience with variable N indicated that usually allowing for variable N slightly modifies but does not change in a fundamental way the results for constant N. Moreover, a recent study by Grimshaw, Pelinovsky & Talipova (2010) shows that for some profiles of $N(z)$, WKB theory gives exactly the right answer. But, of course our results will be more useful if we can extend them to realistic profile of N. Also we limit our problem to finite topography. The topography may have arbitrary shape but it must be localized, i.e. we assume the bottom is flat in the far field.

The paper is organized as follows. In Section 2, we give the governing equations of our problem and specified what we mean by random topography. In Section 3, we derive a formal solution to the scattering problem. An special geometric structure—wave attractor is studied in details in Section 4. And in Section 5 we present our numerical results of the decay of the expected energy flux and compare them with some know results. Conclusions and some discussions are in Section 6.

2 Mathematical formulation

2.1 Govering equations

Our model is two-dimensional (2D) rotating linear Boussinesq system, in which all fields depend on x (horizontal) and z (vertical) only. This does not prevent a non-zero velocity in y-direction due to the Coriolis force. The equations for velocity field $\mathbf{v} = (u, v, w)$, buoyancy b and pressure P are

$$u_t - fv + P_x = 0, \quad v_t + fu = 0, \quad w_t + P_z = b, \quad b_t + N^2 w = 0, \tag{1}$$

and we also need incompressible constraint $u_x + w_z = 0$. For simplicity, assume the Coriolis frequency f and the buoyancy frequency N are constants.

Introducing the stream function $\psi(x,z,t)$ such that $u=\partial_z\psi$, $w=-\partial_x\psi$, we can write Equation (1) as

$$(N^2+\partial_{tt})\partial_{xx}\psi+(\partial_{tt}+f^2)\partial_{zz}\psi=0 \tag{2}$$

For boundary conditions, we use rigid top and bottom boundaries at the ocean surface $z=H$ and the bottom $z=h(x)$

$$\psi(x,H,t)=\psi(x,h(x),t)=0, \tag{3}$$

It is worth mentioning here that the rigid boundary condition on the bottom is not trial and is essential in solving the scattering problem. We focus our attention to the compact region $x\in[-L_x/2,L_x/2]$, and assume the ocean bottom is flat in the far field, i.e. bottom topography $z=h(x)$ is taken to be zero outside the compact region $x\in[-L_x/2,L_x/2]$. For left and right boundaries, we use group velocity to describe the direction of waves, the transmitted waves on the right and reflected waves on the left must obey horizontal radiation condition: energy flux is directed away from the topography. And the incoming waves that enter the region on the left are specified in advance. The geometry of the problem together with the boundary conditions are summarized in Figure 3.

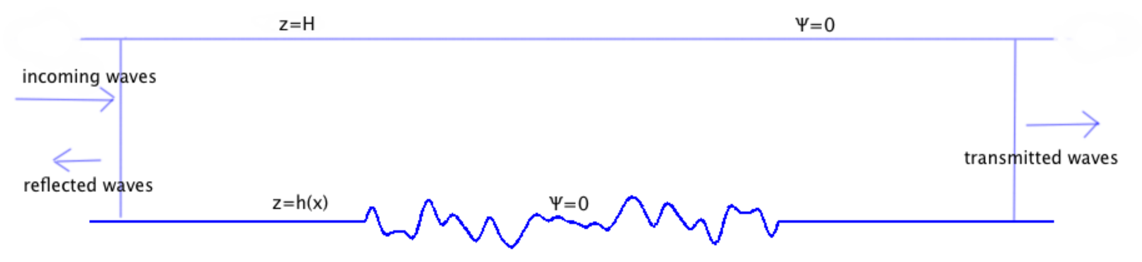

Figure 3: Geometry of the problem and the boundary conditions.

We are interested in time-periodic solutions with given frequency such as the semi-diurnal M_2 tides. And in real ocean $N/f\approx 10$ and $\omega/f\approx 2$ for M_2 tides, hence we assume $f<\omega<N$ and look for solutions of the form

$$\psi(x,z,t)=\mathrm{Re}\Psi(x,z)e^{-i\omega t} \tag{4}$$

where the complex-valued function $\Psi(x,z)$ is to be solved. Then the system is

$$(N^2-\omega^2)\partial_{xx}\Psi-(\omega^2-f^2)\partial_{zz}\Psi=0,\ \ \Psi(x,H)=\Psi(x,h(x))=0 \tag{5}$$

This is one-dimension (1D) wave equation without time-like variable. But we can still solve it by the method of characteristics.

The slope of the characteristics of all internal waves with the same value of frequency ω is at some fixed angle with the vertical, which we rescale to 45^o. In addition, we rescale the ocean depth over the flat bottom to be π and write the non-dimensional variables with a prime as

$$z=\frac{H}{\pi}z',\ \ h=\frac{H}{\pi}h',\ \ x=\frac{1}{\mu}\frac{H}{\pi}x',\ \ \mu=\sqrt{\frac{\omega^2-f^2}{N^2-w^2}} \tag{6}$$

After dropping the prime the non-dimensional equation for Ψ becomes,

$$\Psi_{xx} - \Psi_{zz} = 0, \quad \Psi(x, \pi) = \Psi(x, h(x)) = 0. \tag{7}$$

The bottom topography is called *subcritical*, *critical* or *supercritical* if the non-dimensional topography slope satisfies $|dh(x)/dx| < 1$, $|dh(x)/dx| = 1$ or $|dh(x)/dx| > 1$.

2.2 Random topography

We consider the simplest case of random topography by choosing $h(x)$ for our considered region $x \in [-L_x/2, L_x/2]$ a section of zero-mean stationary Gaussian process defined on the real line by stationary covariance function $C(x)$ such that

$$\mathbb{E}h(x) = 0 \text{ and } \mathbb{E}h(y)h(x+y) = C(x), \tag{8}$$

where $\mathbb{E}$ is the probabilistic expectation. It is easy to generate a complex-valued stationary scalar Gaussian random field $H(x)$ with covariance function $C(x)$ in Fourier space by

$$\hat{H}(k) = \sqrt{\frac{L_x \hat{C}(k)}{2}}(A_k + iB_k) \tag{9}$$

where A_k and B_k are independent Gaussian random variables with mean 0 and variance 1. Then $H = FT^{-1}(\hat{H})$ is a *complex* Gaussian random field satisfying (Yaglom 1962)

$$\mathbb{E}H(y)H(x+y) = C(x). \tag{10}$$

Real-valued field can be generated from complex-valued one by taking real or imaginary part. From our definition, we know if $H = h_1 + ih_2$ is a *complex* Gaussian random field with covariance function $C(x)$, then h_1 and h_2 are independent, *real-valued* Gaussian random fields with covariance function $C(x)/2$ (Hida & Hitsuda 1993). This leads to a nice way of obtaining samples of *real-valued* fields with covariance function $C(x)$, since we only need to generate complex-valued samples with covariance function $2C(x)$ and take their real or imaginary parts.

In Fourier space, we can also compute the covariance function of $h'(x)$ by

$$\mathbb{E}h(y)h(x+y) = C(x) \iff \mathbb{E}h'(y)h'(x+y) = -C''(x). \tag{11}$$

The covariance function $C(x)$ we use for our numerical experiments and its corresponding Fourier transform $\hat{C}(k)$ are

$$C(x) = \sigma^2 \exp\left(-\frac{x^2}{2\alpha^2}\right) \text{ and } \hat{C}(k) = \sqrt{2\pi}\sigma^2\alpha \exp\left(-\frac{k^2\alpha^2}{2}\right) \tag{12}$$

hence we have

$$\mathbb{E}h^2 = C(0) = \sigma^2 \text{ and } \mathbb{E}h'^2 = -C''(0) = \sigma^2/\alpha^2 \tag{13}$$

3 Solving the wave equation

3.1 The method of characteristics and spectrum scheme

In order to solve the wave equation for Ψ,

$$\Psi_{xx} - \Psi_{zz} = 0, \quad \Psi(x, \pi) = \Psi(x, h(x)) = 0, \tag{14}$$

one approach is to follow Muller & Liu (2000a) that use the method of characteristics plus a spectral scheme to satisfy the horizontal radiation condition for scattering waves. This method will fail when characteristic paths converge onto some localized geometric structures that are called wave attractors (see Section 4). Another attractive numerical scheme is using a Green's function approach in which we distribute suitable sources with certain density $\gamma(x)$ along the bottom topography (Echeverri *et al* 2010). Though the method of characteristics has some limitations, we still choose it since it is easy to understand and has a clear physical meaning. And we come out of situations that have wave attractors by discarding such samples in our numerical experiment.

The characteristics of Equation (14) are lines with slope ± 1, i.e. lines along which $x \pm (\pi - z)$are constants. Use the homogeneous boundary condition on the surface $z = \pi$, the general solution is

$$\Psi(x, z) = f(x + z - \pi) - f(x - z + \pi), \tag{15}$$

and the solution is determined if we can solve for the complex-valued function $f(x)$ for all $x \in \mathbb{R}$. It is helpful to think $f(x)$ is defined at every point along the surface and the value of $\Psi(x, z)$ at any interior point can be easily found by tracing both characteristics back to the ocean surface. The non-trial boundary condition $\Psi = 0$ at the bottom $z = h(x)$ implies that for all $x \in \mathbb{R}$, f should satisfy

$$f(x + h(x) - \pi) = f(x - h(x) + \pi). \tag{16}$$

Physically, this means $f(x)$ have the same value at any two points on the surface that can be connected by the characteristics (Figure 4). And $f(x)$ is a periodic function of period 2π in the far field where $h(x) = 0$.

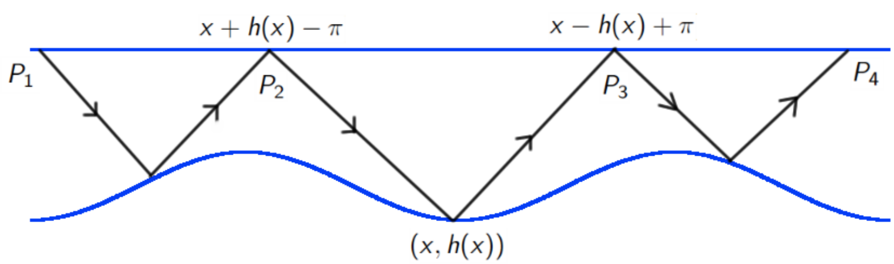

Figure 4: P_1, P_2, P_3 and P_4 are connected by charscteristics so the function f have the same value at these four surface points.

According to the definition from Muller & Liu (2000a), $T(\xi)$ is the surface distance between two characteristics emanating from the same bottom point ξ. The function $T(\xi)$ is called *T-period* and reflects the shape of the bottom topography. For flat bottom, T is 2π. Consider two T-periods T_+ and T_- on each side of the topography in the far field. If we trace a characteristic from one T-period, say T_+, we will end up in either T_+ or T_- in the far field. Hence we can construct a map between T_+ and T_- by tracing a number of characteristics from each period. Since we allow our topography to have supercritical part, T_+ contains a part $T_+^{'}$ which is mapped to T_- and the other part $T_+^{''}$ that is mapped to itself. The same happens to T_-. Therefore $T_+ = T_+^{'} \bigcup T_+^{''}$, and $T_- = T_-^{'} \bigcup T_-^{''}$ such that $T_+^{'}$ is mapped onto $T_-^{'}$, $T_+^{''}$ onto itself, $T_-^{'}$ onto $T_+^{'}$ and $T_-^{''}$ onto itself. And we denote the map from T_+ by $\mathcal{M}$ and the map from T_- by $\mathcal{M}^{-1}$. To be more explanatory, we depict the situation in Figure 5.

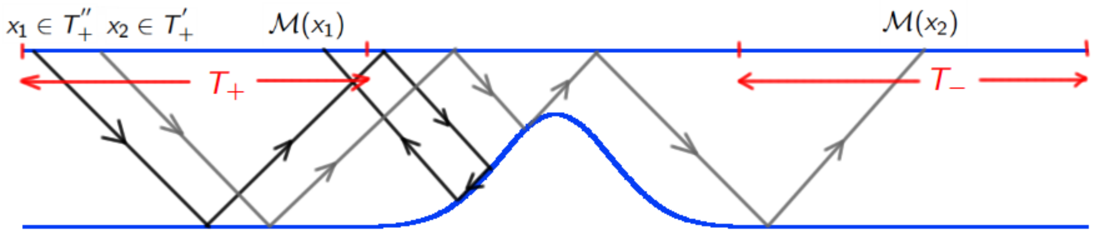

Figure 5: This graph shows how we define T_+, T_-, $T_+^{\prime}$ and $T_+^{\prime\prime}$. Similar definition applies to $\mathcal{M}^{-1}$ except that characteristics start from T_-. Characteristic can be reflected back by supercritical part of the bottom (compare with Figure 4). Bottom topography is $2e^{-x^2/2}$.

The top and bottom boundary conditions imply that

$$f(\mathcal{M}(x)) = f(x) \text{ if } x \in T_+, \quad f(\mathcal{M}^{-1}(x)) = f(x) \text{ if } x \in T_-. \tag{17}$$

And to be more physical, we decompose the complete wave fields in the far field by

$$f(x) = f^0(x) + f^r(x),\ x \in T_+, \quad f(x) = f^t(x),\ x \in T_- \tag{18}$$

where $f^0(x)$ for incoming waves, $f^r(x)$ for backward reflected waves and $f^t(x)$ for forward transmitted waves. More specifically, with the periodic condition (17) we have

$$f^0(x) + f^r(x) = \begin{cases} f^t(\mathcal{M}(x)) & x \in T_+^{'}, \quad \mathcal{M}(x) \in T_-^{'} \\ f^0(\mathcal{M}(x)) + f^r(\mathcal{M}(x)) & x \in T_+^{''}, \quad \mathcal{M}(x) \in T_+^{''} \end{cases} \tag{19}$$

$$f^t(x) = \begin{cases} f^0(\mathcal{M}^{-1}(x)) + f^r(\mathcal{M}^{-1}(x)) & x \in T_-^{'}, \quad \mathcal{M}^{-1}(x) \in T_+^{'} \\ f^t(\mathcal{M}^{-1}(x)) & x \in T_-^{''}, \quad \mathcal{M}^{-1}(x) \in T_-^{''}. \end{cases} \tag{20}$$

As mentioned earlier, in the far field over zero bottom topography, f^0, f^r and f^t are periodic functions with period 2π. Hence we can expand them as Fourier series and because of the radiation condition they have the form

$$f^0(x) = \sum_{k=1}^{\infty} a_k^0 e^{ikx}, \quad f^r(x) = \sum_{k=0}^{\infty} a_k^r e^{-ikx}, \quad f^t(x) = \sum_{k=1}^{\infty} a_k^t e^{ikx}. \tag{21}$$

Without loss of generality, we can set $a_0^t = 0$, since the two constant terms a_0^r and a_0^t enter our problem in the form $a_0^r - a_0^t$. If we substitute the Fourier representation (21) into the periodic condition and project onto the mth Fourier mode , we obtain a linear system

$$\mathbf{a}^r = B\mathbf{a}^t + T\mathbf{a}^0 + A\mathbf{a}^r, \tag{22}$$

$$\mathbf{a}^t = S\mathbf{a}^0 + D\mathbf{a}^r + C\mathbf{a}^t. \tag{23}$$

where the coefficient matrices are given by

$$B_{mk} = \frac{1}{2\pi}\int_{T'_+} e^{ik\mathcal{M}(x)}e^{imx}dx \qquad m = 0,1,2,\cdots \quad k = 1,2,3,\cdots$$

$$T_{mk} = \frac{1}{2\pi}\int_{T''_+} e^{ik\mathcal{M}(x)}e^{imx}dx \qquad m = 0,1,2,\cdots \quad k = 1,2,3,\cdots$$

$$A_{mk} = \frac{1}{2\pi}\int_{T''_+} e^{-ik\mathcal{M}(x)}e^{imx}dx \qquad m = 0,1,2,\cdots \quad k = 1,2,3,\cdots$$

$$S_{mk} = \frac{1}{2\pi}\int_{T'_-} e^{ik\mathcal{M}^{-1}(x)}e^{-imx}dx \qquad m = 1,2,3,\cdots \quad k = 1,2,3,\cdots$$

$$D_{mk} = \frac{1}{2\pi}\int_{T'_-} e^{-ik\mathcal{M}^{-1}(x)}e^{-imx}dx \qquad m = 1,2,3,\cdots \quad k = 1,2,3,\cdots$$

$$C_{mk} = \frac{1}{2\pi}\int_{T''_-} e^{ik\mathcal{M}^{-1}(x)}e^{-imx}dx \qquad m = 1,2,3,\cdots \quad k = 1,2,3,\cdots$$

We can solve this linear system by truncating at a certain number of modes, and find the solution once the mapping functions $\mathcal{M}$ and $\mathcal{M}^{-1}$ are known.

3.2 Checkerboard map

In order to construct the mapping function $\mathcal{M}$ and $\mathcal{M}^{-1}$, we only need to know how to decide the 'next' point x_{k+1} if given a point x_k on the surface. We can do this by tracing characteristics. However, there are two characteristics start from every surface point. This leads us to an ambiguous situation that we have two candidates for x_{k+1}. Figure 6 illustrates the double-valued situation for a chosen bottom topography $h(x) = 2e^{-x^2/2}$. We need a way to get rid of the double-valued mapping.

Manually we can distinguish these two candidates once we know the starting direction of the characteristic we need to follow. On a computer, we adopt the checkerboard construction by Balmforth *et al.* (1995) to track the direction of the characteristic. To be specific, we focus our attention on the bottom region $-L < x < L$ containing the random topography ($L > L_x/2$). For right-going and left-going characteristics define the new mapping variable as $x' = x+L$ and $x' = x-L$, respectively. Therefore, the new mapping variable for reflection points of right-going characteristics are positive while negative for left-going characteristics. So we have a way that automatically keep track of the characteristics' directions. Figure 7 shows the checkerboard map for Gaussian bump $h(x) = 2e^{-x^2/2}$. Comparing with Figure 6, we can see that by introducing the new shifted variable we get the desired $1:1$ map.

We can see from Figure 7, the checkerboard map for topography with supercritical part is discontinuous. The discontinuities come from critical points where the absolute value

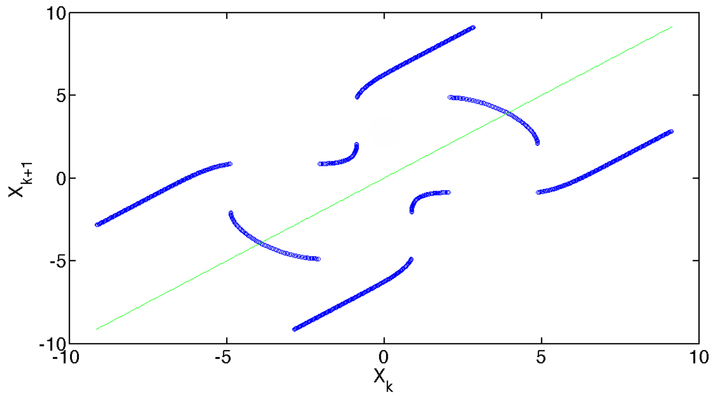

Figure 6: Double-valued map for bottom $h(x) = 2e^{-x^2/2}$.

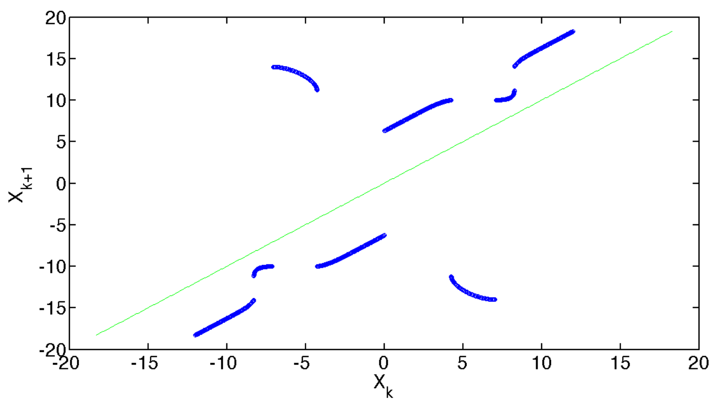

Figure 7: Checkerboard map for bottom $h(x) = 2e^{-x^2/2}$.

of topography slope change from bigger than 1 to smaller than 1. Figure 8 shows how discontinuities occur when characteristics hit critical points.

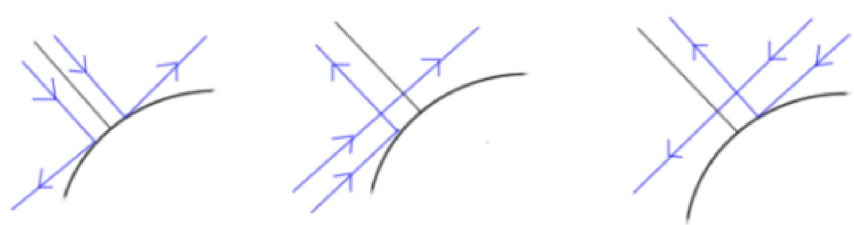

Figure 8: Three cases that can lead to discontinuities for critical points with positive derivatives. Similar cases for critical points with negative derivatives.

It is much more difficult to build the checkerboard map with supercritical topography. Unlike the purely subcritical situation in which characteristic can only go forward and only hits the bottom once between neighboring surface points, characteristic can be reflected back by the supercritical part of the bottom topography and hits several bottom points before it reaches the surface again. Hence we are in a rather complicated situation in letting the computer know which characteristic to follow while also need to solve for the intersections of characteristics and the bottom (this is the most time-consuming part in numerical experiments). We need to switch to another characteristic at these intersection points. Figure 9 shows all the eight cases that could happen when characteristics intersect with the bottom and indicates the characteristic we should choose.

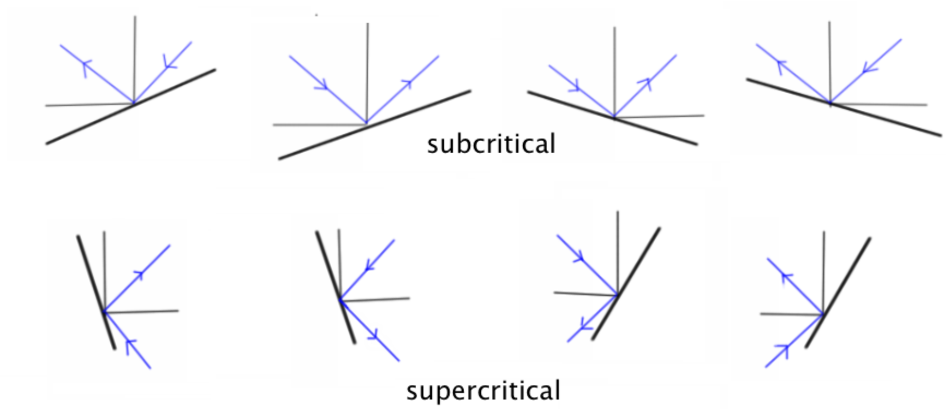

Figure 9: Eight Cases that could happen when characteristics intersect with the bottom.

Allowing the bottom topography to have supercritical part makes the problem more complicated. Can we only consider subcritical case? Some models have been built to describe the shape of the bottom topography. One of them is the analytic spectrum created by Bell (1975). This is an estimate of the power spectrum based primarily on topographic data from the abyssal hill region of the ocean basin in the eastern central North Pacific. And the bottom topography is modeled as a random distribution of statistically independent hills. The spectrum is defined such that the variance of the dimensional height $\tilde{h}(x, y)$ is

$$\mathbb{E}\tilde{h}^2 = \frac{\pi}{2}\int_0^{k_c} \frac{F_0 k}{(k^2+k_0^2)^{3/2}} dk \approx (125m)^2 \tag{24}$$

where $F_0 = 250m^2$ cycles km^{-1}, $k_0 = 0.025$ cycles km^{-1} and the effective cut-off wave number $k_c = 2.5$ cycle km^{-1}. The variance of the slope is

$$\mathbb{E}|\nabla\tilde{h}|^2 \approx (125m)^2 k_0 k_c \approx 0.2^2. \tag{25}$$

This is the spectrum for 2D topography. In order to apply it to our 1D topography, we need to assume the topography is isotropic, i.e. assuming each of the two parts of the derivative $|\nabla\tilde{h}|^2 = \tilde{h}_x^2 + \tilde{h}_y^2$ has the same expected value. Therefore, the 1D model topography has

$$\mathbb{E}|\tilde{h}'|^2 \approx (125m)^2 k_0 k_c/2 \approx 0.14^2. \tag{26}$$

The typical value of the slope of characteristics before non-dimensionalization is $\mu = 0.17$. So if we assume the bottom is modeled as a zero-mean stationary Gaussian process, the supercritical part takes up about 22.5% of the ocean bottom, which implies that the supercritical part shouldn't be neglected.

Although there is evidence that the ocean topography is not strictly isotropic, measurements of eastern central North Pacific may not be able to represent the whole sea topography and more recent models are proposed by Goff & Jordan (1988) and Nikurashin & Ferrari (2010), our consideration of supercritical part is still reasonable. As we mentioned earlier, the supercritical part of the topography makes the checkerboard map discontinuous. The discontinuities could probably lead to significant differences. And we will see in Section 4 that even when the topography contains only a small part of supercritical bottom, say about 5%, there can be wave attractors especially for long topography, which can never happen for purely subcritical bottom.

4 Wave Attractors

In this section, we look at a special geometric structure of the characteristics. As the characteristic can be reflected back by the supercritical part of the bottom, it is possible that the characteristic forms some closed orbits, what is called *wave attractors*. One reason we want to look at wave attractors is that if there are attractors, our method of tracing characteristics to get the map $\mathcal{M}$ and $\mathcal{M}^{-1}$ will fail. Since our path following the characteristics will probably converge onto the closed orbit and can never reach either T-period in this case. We certainly can use other numerical methods such as the Green's function to solve our 1D wave equation. But the wave attractors are still of great interest since their existence can lead to significant different behavior of internal waves. Figure 10 (from Echeverri *et al.* 2011) describes such a situation. The horizontal axis is a parameter value that describes the bottom topography and the vertical axis is the conversion rate that measures how much energy in the barotropic tides is converted to the energy of internal waves. This is related to our problem because this conversion of energy provides a way of realizing the incoming waves. And we can see that the existence of attractors even leads to an ill-posed problem because the numerical results do not converge when increasing the resolution.

4.1 Example of wave attractors

We can have different kinds of wave attractors. And we classify them by the number of reflection points of the closed orbit on the surface. The simplest case is 1-point attractor as shown in Figure 11. The bottom topography is given by $h(x) = B\left(1 - \cos\left(\frac{2\pi x}{A}\right)\right),\ |X| \leqslant A$ and 0 elsewhere. The parameter values are $B = 1.15$ and $A = 1.6\pi$. We can also consider the stability of these closed orbits, i.e. whether the characteristic paths converge onto them. Since our problem involves mapping from both directions and the characteristic path is reversible, these closed orbits must be stable from one direction and unstable from the other. For 1-point attractor, the stability can be easily determined by examine whether the fixed point of the map $X_{k+1} = F(X_k)$ is stable or not. As shown in Figure 11, the stable orbit for clockwise characteristic path is indicated by arrows, whereas the other is unstable.

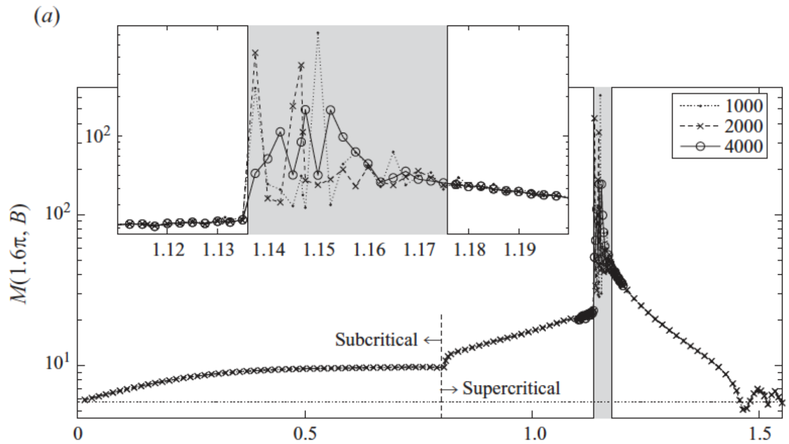

Figure 10: Conversion rates for $h(x) = B\left(1 - \cos\left(\frac{2\pi x}{A}\right)\right)$, $|X| \leqslant A$ and 0 elsewhere. The parameter values are $B = 1.15$ and $A = 1.6\pi$. And three truncations are shown: $K = N = 1000$, 2000 and 4000. This Figure is taken from P. Echeverri *et al*, 2011.

Because of the symmetry of the topography, there are two corresponding closed orbits for counterclockwise characteristic path, and the stability of the two orbits is interchanged.

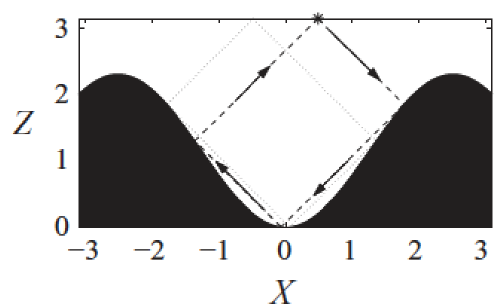

Figure 11: The bottom topography is given by $h(x) = B\left(1 - \cos\left(\frac{2\pi x}{A}\right)\right)$, $|X| \leqslant A$ and 0 elsewhere, where $B = 1.15$ and $A = 1.6\pi$. Stable orbit for clockwise characteristic path is indicated by arrows. This Figure is taken from P. Echeverri *et al*, 2011.

We can also have 2-point wave attractor, actually this is the most common kind of attractors we find in our numerical simulations (see Section 4.3). Figure 12 is a 2-point wave attractor. Red dots on the surface indicate the location of reflection points of the characteristic path while the black line is the corresponding closed orbit. The stability of multi-point wave attractors is geometrically more complicated since we need to consider all surface points. So we do not go into details here. We can have more than two reflection points on the surface, Figure 13 is an example of 4-point wave attractor founded in our numerical simulations.

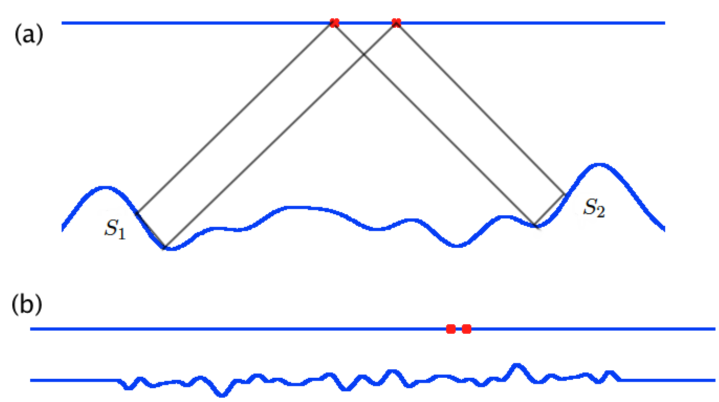

Figure 12: (a) A sample that has 2-point wave attractor in numerical simulations with parameter value $\sigma = 0.25$, $\alpha = 0.5$ for zero-mean stationary Gaussian random field generated by covariance function in Equation (12). S_1 and S_2 are two supercritical points, while other points are subcritical. The whole plot of the random bottom topography is shown in (b). The length of random bottom is 10π.

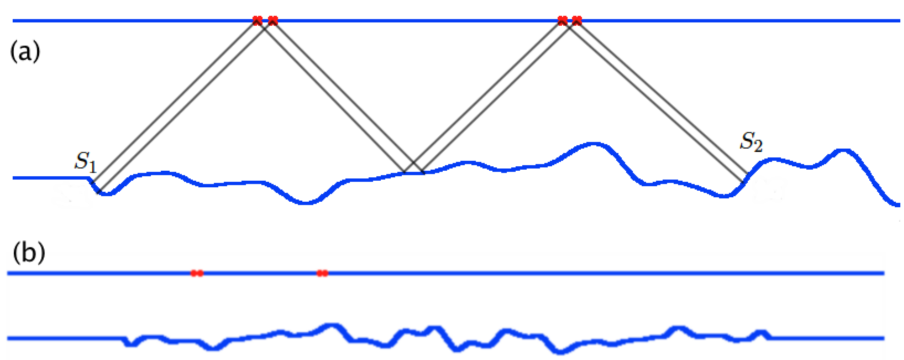

Figure 13: A sample that has 4-point wave attractor in numerical simulations with parameter value $\sigma = 0.25$, $\alpha = 0.5$ for zero-mean stationary Gaussian random field generated by covariance function in Equation (12). S_1 and S_2 are two supercritical points, while other points are subcritical. The whole plot of the random bottom topography is shown in (b). The length of random bottom is 10π.

4.2 Method to detect attractors

Finding 1-point wave attractor is just finding the fixed point for the checkerboard map. To find the fixed point, we only need to check whether the checkerboard map and the straight line $x_k = x_{k+1}$ have any intersection. In Figure 14, we find 4 intersections, and they correspond to the two closed orbits (in Figure 11) in both directions.

To find 2-point attractor, a natural way is to apply the checkerboard map forward two

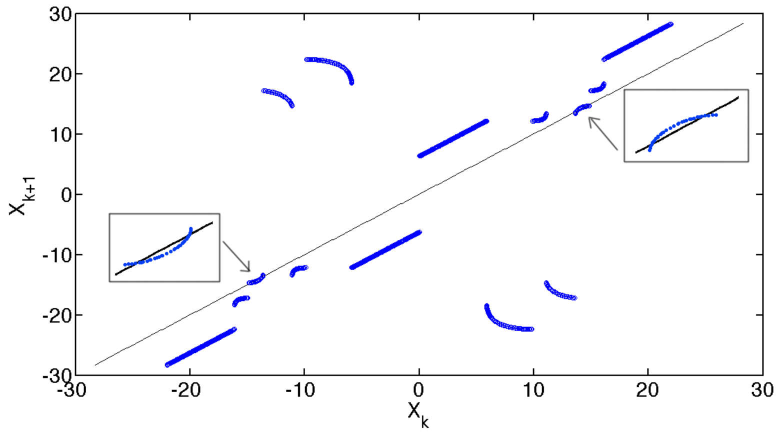

Figure 14: Checkerboard map for topography $h(x) = B\left(1 - \cos\left(\frac{2\pi x}{A}\right)\right), \quad |X| \leqslant A$, with parameter value $B = 1.15$ and $A = 1.6\pi$. Two magnifications show the structure near the two fixed points

times and then find the fixed points of the map $X_{k+2} = F(X_k)$. However, this method has some shortcomings. Since it is impossible to build checkerboard map for every single point on the surface, we actually build the checkerboard map by discretizing the bottom and then tracing characteristics emanating from every discretized point until they reach the surface. For arbitrary surface point we find its checkerboard map by linear interpolation while keeping an eye on the discontinuities. This process unavoidably leads to some numerical error. Since attractors are delicate structures that are sensitive to errors, this is not the best idea. An alternative way is to find the intersection points of the checkerboard map with the backward checkerboard map $X_{k-1} = G(X_k)$. This method is better because we do not need to find the discontinuities of the map $X_{k+2} = F(X_k)$ and apply linear interpolation, both time saving and with less numerical error. Backward checkerboard map can be easily obtained by just reversing the order of the two coordinates. We use this method to find 2-point wave attractors in our numerical experiments and Figure 15 is the checkerboard map for one particular sample.

Similar ways can be used to find wave attractors involving more reflection points on the surface. Just as the situation for 2-point wave attractor, we don't apply the checkerboard map four times to find the fixed points of the map $X_{k+4} = F(X_k)$ due to potential numerical errors. Instead, we apply the checkerboard map twice and seek the intersection points of the map $X_{k+2} = F_1(X_k)$ with $X_{k-2} = F_2(X_k)$. Again, the map $X_{k-2} = F_2(X_k)$ can be easily found by interchanging the two coordinates of the map $X_{k+2} = F_1(X_k)$. Figure 16 shows the checkerboard map for a sample that have 4-point wave attractor in our numerical simulations.

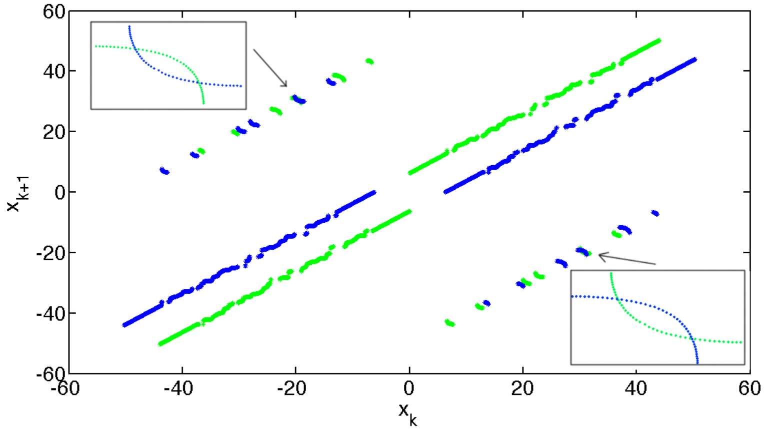

Figure 15: One sample that has 2-point wave attractor with parameter value $\sigma = 0.25$ and $\alpha = 0.5$ for zero-mean stationary Gaussian random field generated by covariance function in Equation (12). The length of random topography is 10π. Magnifications are used to show the structure near the intersection points.

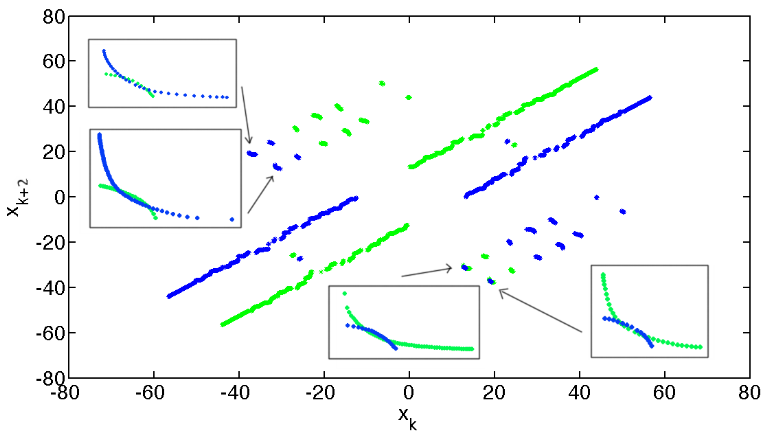

Figure 16: One sample that has 4-point attractor with parameter value $\sigma = 0.25$ and $\alpha = 0.5$ for zero-mean stationary Gaussian random field generated by covariance function in Equation (12). The length of random topography is 10π. Magnifications show the structure near the intersection points.

4.3 Probability of having attractors

In order to get an idea of the probability of having wave attractors, we do several numerical experiments. Here we only look at wave attractors that involving $1 \sim 4$ reflection points. More complicated attractors are possible but because of the finite length of the random topography we use (10π in our numerical simulations) and their more complicate structures, these attractors are of very low probability.

We choose the parameter $\sigma = 0.06$, 0.10, 0.13, 0.17, 0.21 and 0.25 while keeping $\sigma/\alpha = 1/2$ fixed. For this fixed value we can easily estimate the probability of supercritical bottom. Since we model the bottom topography as a section of zero mean stationary Gaussian process, the absolute value of the slope of the bottom is bigger than 1 if and only if it is larger than two standard deviations of the slope, which is σ/α by Equation (13). Therefore about 4.55% of the bottom is supercritical. We plot the results in Figure 17(a), and the probability is calculated for 1000 simulations.

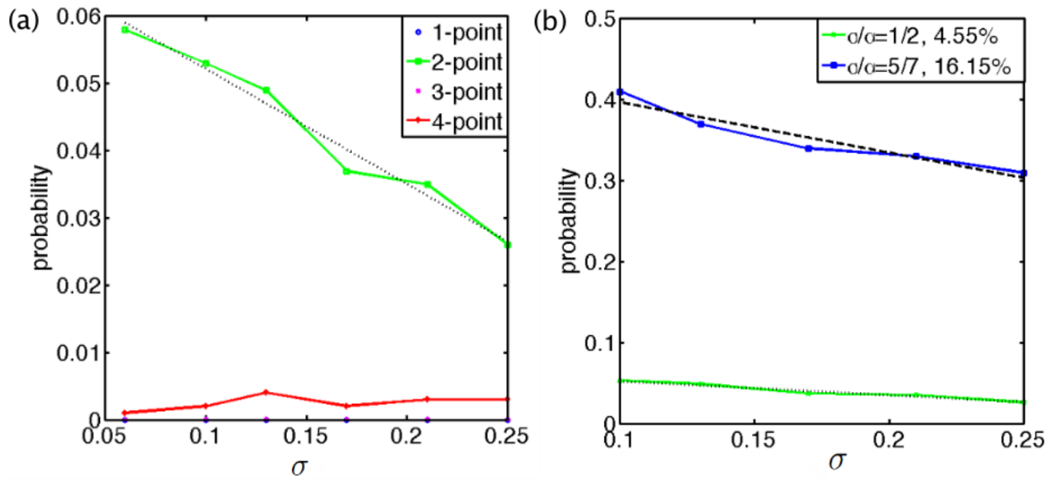

Figure 17: (a) Probability of having attractors for parameter $\sigma = 0.06$, 0.10, 0.13, 0.17, 0.21 and 0.25 with fixed $\sigma/\alpha = 0.5$ in 1000 simulations. (b) Probability of having 2-point attractors for $\sigma/\alpha = 1/2$ (1000 simulations) and $\sigma/\alpha = 5/7$ (100 simulations). The supercritical part is about 4.55% and 16.15% of the random topography, which is of length 10π.

From the graph, we can see there is no 1-point or 3-point attractor. Here is a simple explanation for this. Let $\triangle = \max|h(x)|$ the largest deviation of height, then the distance from P_1, P_2 and B to the surface are given by $H_{P_1} = \pi + \alpha\triangle$, $H_{P_2} = \pi + \beta\triangle$ and $H_B = \pi + \gamma\triangle$ while α, β and γ are parameters that varying between -1 and 1. From Figure 18, these three distances have a very nice relation,

$$H_{P_1} + H_{P_2} = H_B.$$

By simple algebra, we have $3\triangle > (\gamma - \alpha - \beta)\triangle = \pi$, which leads to

$$\triangle > \pi/3 \text{ or correspondingly } \sigma > \pi/9 \approx 0.35$$

since we model the topography by Gaussian process. Similar argument suggests we need $\triangle > \pi/5$ or $\sigma > \pi/15 \approx 0.21$ to have 3-point attractor. Hence for small-amplitude topography we are interested in, there is no 1-point or 3-point attractor.

The probability of having 2-point attractors increases as the value of σ decreases. This is because when we reduce the value of σ, the width of each bump also decreases. So we

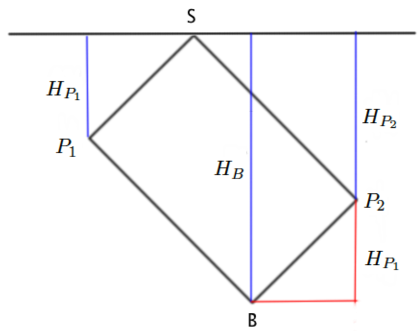

Figure 18: Showing the relation between H_{P_1}, H_{P_2} and H_B. P_1 and P_2 are two supercritical points, B is usually but not necessarily a point on the bottom while S is the surface reflection point.

tend to have more intervals and therefore more supercritical intervals. By examining the structure of 2-point attractor as in Figure 12(a), we can see that we need two supercritical points S_1 and S_2 to form the closed orbit. And they must belong to different supercritical intervals. The length of each supercritical interval may be an issue, but since what we need is only supercritical points S_1 and S_2, we can assume the length do not have a significant effect on the probability. So if we have more supercritical intervals we tend to have a higher probability of finding 2-point attractors.

Similar arguments can also apply to 4-point attractor, because in order to form 4-point attractor, we also need two supercritical points S_1 and S_2 in different supercritical intervals. This implies the probability should increase when we reduce σ. However, from Figure 18, the probability of 4-point attractors does not show the expected increase. Two reason might account for this. One is the statistical error. From the graph, the existence of 4-point attractors is a rare event, we only get roughly 2 or 3 4-point attractors in 1000 simulations. So the probability of 4-point attractors in these 1000 samples is not convincing. We need more simulations to know how the probability changes with σ. Numerical errors may also have an effect on the total number of 4-point attractors. Although we only apply the checkerboard map twice, there is still some numerical error due to linear interpolation. And attractors are delicate structures and sensitive to numerical errors.

By Figure 17(a), the probability of having 4-point attractors is much less than that of 2-point attractors. Finite length of the topography is one reason, since if considered small amplitude topography the distance between the two supercritical points S_1 and S_2 is roughly 2π for 2-point attractor and 4π for 4-point attractor. And also to form 4-point attractor, we need 6 points in the right place while we only need 4 for 2-point attractor.

We fix $\sigma/\alpha = 5/7$ which will increase the probability of supercritical part to about 16.15%, and only look at the probability of 2-point attractors for parameter value $\sigma = 0.10$, 0.13, 0.17, 0.21 and 0.25 within 100 simulations. According to our arguments that more supercritical intervals leads to higher probability of having 2-point attractors, we expect higher probability of 2-point attractors than the case for $\sigma/\alpha = 1/2$, about 4.55% supercritical part of the topography. This is confirmed in Figure 17(b). Also from the graph, the relation between the value of σ and the probability is roughly linear. But we do not have an explanation for this so far.

5 Energy Decay

The problem we are aiming for in this project is the energy decay of internal waves caused by scattering over rugged sea-floor topography, i.e. if given mode-one incoming waves, we want to know how much energy is left in the first mode of the transmitted waves. Due to the existence of wave attractors, we only study samples without attractors by throwing away samples that contain attractors.

For random subcritical topography, there is clear evidence that the expected energy flux has exponential decay (Bühler & Holmes-Cerfon 2011) and the decay rate is defined as

$$E_1(n) = \mathbb{E}|a_1^t|^2 = e^{-\lambda_1 n}. \tag{27}$$

where n is the number of bounces on the bottom. Though not being able to derive a rigorous formula for the decay rate λ_1, they suggest an expression for λ_1 of the form

$$\lambda_1 = \sum_{k=1}^{+\infty} k\hat{C}(k), \tag{28}$$

where $\hat{C}(k)$ is the Fourier transform of the covariance function $C(x)$. And a simpler form is valid for uncorrelated ($|C(x)| \ll C(0)$ for $x \geqslant 2\pi$) topography

$$\lambda_1 = \Gamma_0\sqrt{\mathbb{E}|h|^2\mathbb{E}|h'|^2} = \Gamma_0\sigma^2/\alpha, \tag{29}$$

with $\Gamma_0 = 2.5$ for Gaussian covariance function.

Our guess is that we still have exponential decay of energy flux for topography with supercritical part. To test our guess, we fix $\sqrt{\mathbb{E}|h|^2\mathbb{E}|h'|^2} = \sigma^2/\alpha$ since for small α, the correlation length, which is proportional to α, is small so our topography remains roughly uncorrelated. And we use $n = L_x/2\pi$ as our variable, where L_x is the length of the random bottom topography. The parameter value we use is summarized in Table 1 and the results is given in Figure 19. The logarithmic plot clearly indicates decay of expect energy flux. (a) gives a better result than (b) mainly because the parameter α is smaller, which mean smaller correlation length and better approximation of formula (29).

σ^2/α	σ	α	supercritical part
1/22	0.10	0.22	2.79%
1/22	0.09	0.1782	4.77%
5/48	0.25	0.60	1.64%
5/48	0.20	0.384	5.49%
5/48	0.17	0.27744	10.27%

Table 1: The parameter value we use for numerical simulations.

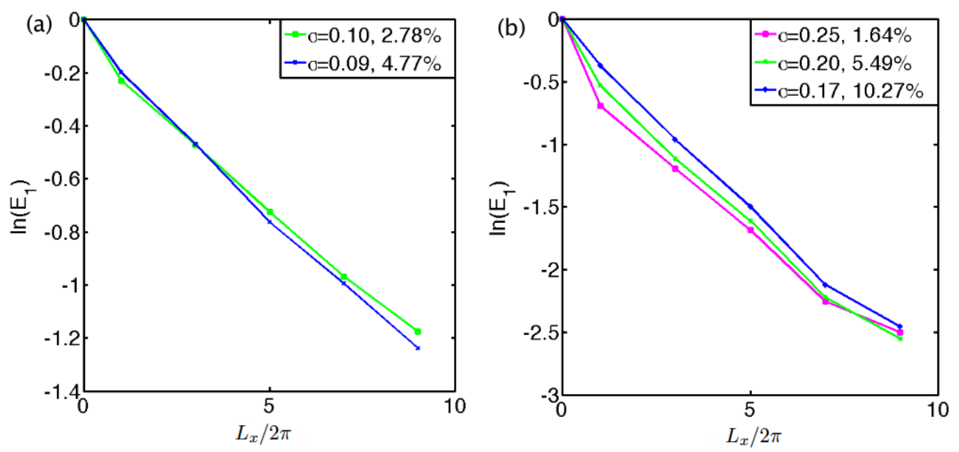

Figure 19: $\sigma^2/\alpha = 1/22$ and $5/48$, respectively. $\sigma = 0.10$, 0.09, 0.25, 0.20 and 0.17. The expectation at each point is taken to be the average over $N = 50$ topography samples without attractors.

We can use least square method to linearly fit (Figure 20) our data points, for $\sqrt{\mathbb{E}|h|^2\mathbb{E}|h'|^2} = \sigma^2/\alpha = 1/22$ and $5/48$, we get $\lambda_1 \approx 0.132$ and 0.275, respectively. And we can compare the decay rate we get from numerical simulations with theoretical prediction given by formula (29). The results are collected in Table 2.

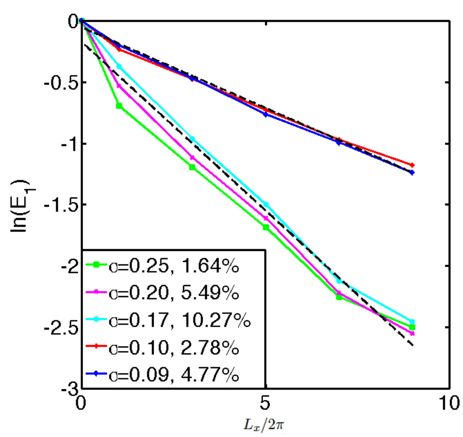

Figure 20: Linearly fit the data points by least square method.

6 Conclusion and discussions

In this project, we find a way to build checkerboard map for arbitrary smooth topography. After being able to obtain the checkerboard map we look at a spacial geometric structure–

σ^2/α	λ_1	$\lambda_1^* = \Gamma_0\sigma^2/\alpha$	$(\lambda_1 - \lambda_1^*)/\lambda_1 \times 100\%$
1/22	0.132	5/44	13.9%
5/48	0.275	25/96	5.30%

Table 2: λ_1 is the decay rate we get from numerical simulations. λ_1^* is the predicted decay rate taken from formula (29). The last column is the relative error.

wave attractor. We find some factors that can influence the probability of having attractors and give qualitatively explanation of them. But rigorous explanation is still missing. The geometric structure of the closed orbits, especially those involving more than one surface reflection points is complicated. So coming up with exact formula for the probability of multi-point attractor is difficult when the topography is generated randomly.

Also our method of finding attractors relies heavily on the checkerboard map. As mentioned in Section 3.2, obtaining the checkerboard map for supercritical topography is not easy and time consuming, so we are limited to rather short topography length (10π in our numerical simulations). Can we find a way to detect wave attractor without using the checkerboard map? After all, the topography is totally determined by its Fourier coefficients $\hat{h}(k)$. So $\hat{h}(k)$ should have some special properties to put several points in the exactly right place to form closed orbit.

We also look at decay of energy flux by using the simplest formula (29) because we can clearly see how our parameter σ and α relate to the decay rate λ_1. Also due to the difficulties in building checkerboard map, we only look at rather short topography length, say $L_x < 9 \cdot 2\pi$. Numerical error is still an issue, since for finding the maps $\mathcal{M}$ and $\mathcal{M}^{-1}$, we need to interpolate the checkerboard map several times. The existence of wave attractors forces us to discard samples that have attractors, since our current method can not deal with cases that have attractors. We need other numerical schemes, such as the Green's function to include sample with attractors. And we also need to add a little viscosity to put forward a well-posed problem. Another reason that we do not consider sample with attractors is that the existence of attractors might lead to significant different energy decay mechanism, just like what happens in Figure 10. And we can't explain the exponential decay rigorously.

7 Acknowledgments

This project is done in the Geophysical Fluid Dynamics Program at Woods Hole Oceanographic Institution. I want to thank directors of this year Charles Doering, Oliver Bühler and Colm Caulfield for organizing such a wonderful program. I would also like to thank my summer supervisor Miranda Holmes-Cerfon for her great patience, valuable advice and indispensable help during the whole summer. And of course, special thanks to Prof. Oliver Bühler for recommending me such a nice summer program.

References

[1] BALMFORTH, N. J., SPIEGEL, E. A. & TRESSER, C. 1995 Checkerboard maps. *Chaos* **5**(1), 216-226

[2] BELL, T. H. 1975 Statistical features of sea-floor topography. *Deep-Sea Res.* **22**(12), 883-892.

[3] BÜHLER, O. & HOLMES-CERFON, M. 2011 Decay of an internal tide due to random topography in the ocean. *J. Fluid Mech.* **678,** 271-293.

[4] ECHEVERRI, P., YOKOSSI, T., BALMFORTH, N. J., & PEACOCK, T. 2011 Tidally generated internal-wave attractors between double ridges. *J. Fluid Mech.* **669,** 354-374.

[5] GOFF, J. & JORDAN, T. 1988 Stochastic modeling of seafloor morphology: inversion of sea beam data for second-order statistics. *J. Geophys. Res.* **93** (B11), 13589-13608.

[6] GRIMSHAW, R., PELINOVSKY, E. & TALIPOVA, Y. 2010 Nonreflecting internal wave beam propagation in the deep ocean. *J. Phys. Oceanogr.* **40**(4), 802-813.

[7] HIDA, T. & HITSUDA, M. 1993 Gaussian processes, representation and applications. *Amer. Math. Soc.*

[8] HOLMES-CERFON, M. personal notes on generating stationary Gaussian random fields.

[9] MASS, L. R. & LAM, F. P. 1995 Geometric focusing of internal waves. *J. Fluid Mech.* **300,** 1-41.

[10] MÜLLER, P. & LIU, X. B. 2000a Scattering of internal waves at finite topography in two dimensions. Part I. Theory and case studies. *J. Phys. Oceanogr.* **30**(3), 532-549.

[11] NIKURASHIN, M., & FERRARI, R. 2010 Radiation and dissipation of internal waves generated by geotropic motions impinging on small-scale topography: application to the southern ocean. *J. Phys. Oceanogr.* **40**, 2025-2042.

[12] YAGLOM, A. M. 1962 An introduction to the theory of stationary random functions. *Dover.*